Magnetostructural relationship in the tetrahedral spin-chain oxide $CsCoO_2$

N. Z. Ali,[1] R. C. Williams,[2,*] F. Xiao,[2] S. J. Clark,[2] T. Lancaster,[2] S. J. Blundell,[3] D. V. Sheptyakov,[4] and M. Jansen[1]

[1]*Max-Planck-Institut für Festkörperforschung, Heisenbergstraße 1, D-70569 Stuttgart, Germany*

[2]*Department of Physics, Durham University, South Road, Durham, DH1 3LE, United Kingdom*

[3]*Department of Physics, Oxford University, Parks Road, Oxford, OX1 3PU, United Kingdom*

[4]*Laboratory for Neutron Scattering and Imaging, Paul Scherrer Institut, CH-5232 Villigen, Switzerland*

(Received 13 October 2014; revised manuscript received 15 December 2014; published 20 January 2015)

We have investigated the structural and magnetic transitions in $CsCoO_2$ using calorimetric measurements, neutron powder diffraction, density functional theory calculations, and muon-spin relaxation measurements. $CsCoO_2$ exhibits three-dimensional long-range antiferromagnetic (AFM) order at 424 K, resulting in antiferromagnetic alignment of chains of ferromagnetically ordered Co-Co spin dimers. Although there is no change in magnetic structure around a structural transition at $T^* = 100$ K, the resulting bifurcation of corner-shared Co-O-Co bond angles causes a weakening of the AFM interaction for one set of bonds along the chains. Consequently, the system undergoes a complex freezing out of relaxation processes on cooling.

DOI: 10.1103/PhysRevB.91.024419 PACS number(s): 75.30.Et, 75.50.Ee, 76.75.+i

I. INTRODUCTION

Cobalt-based multinary oxides continue to attract significant interest due to their complex phase diagrams and the richness of their magnetic and electronic properties, induced by strong correlation between spin, charge, and orbital degrees of freedom. Together with chemical composition and synthesis conditions, the spin states in oxocobaltates are sensitive to external physical parameters such as temperature and pressure. A subtle energy balance between the crystal field splitting and Hund's rule exchange energy in the $3d$ states ultimately regulates the spin state of individual Co ions, offering new potential for tuning materials properties [1–3]. The most commonly encountered coordination geometry in multinary oxocobaltates(III) is octahedral, resulting in the low-spin $3d^6$ electron configuration ($S = 0$; $t_{2g}^6 e_g^0$). The less commonly observed tetrahedral coordination geometry, with the weaker crystal field splitting, favors the high-spin state ($S = 2$; $e_g^3 t_{2g}^3$) [4–8]. Within the AMO_2 family of ternary oxides, the recently discovered $CsCoO_2$ features a singular crystal structure [9]. Here Co^{3+} is again in a tetrahedral coordination with edge-linked CoO_4 tetrahedra forming "bow-tie"-shaped $Co_2O_6^{6-}$ dimers which are then connected via corner-shared oxygen ions to form spin chains, creating an overall butterfly motif.

The special connectivity engendered by this architecture leads to very strongly coupled antiferromagnetism. According to the Goodenough-Kanamori-Anderson (GKA) rules the interdimer superexchange interaction (mediated via corner-shared oxygen ions, denoted O2) the Co-O2-Co bonding angle between neighboring Co atoms lies close to 180°; hence the subsequent interaction between partially filled d orbitals is strongly anitferromagnetic (AFM). Conversely, intradimer Co-Co neighbors are coupled through the intervening edge-shared oxygen ions (denoted O1) with bonding angles close to 90°, and hence the superexchange interaction is expected to be ferromagnetic (FM). Measurements of the magnetic susceptibility [9] show that the consequence of the connectivity between Co^{3+} ions in such a structure is canted antiferromagnetic order below the remarkably high temperature of $T_N = 430$ K. Above the ordering temperature the susceptibility becomes temperature independent, suggesting the persistence of very strong exchange coupling. Despite the progress made in understanding this system, the magnetic behavior that accompanies a structural transition that occurs around 100 K (hereafter denoted $T^\star$), involving a monoclinic distortion resulting from a tilting of the edge-sharing tetrahedra, remains poorly understood. We have therefore carried out a detailed investigation into the magnetism of this system, whose aim is to determine the low energy model of spin interactions and to elucidate both the nature of the ordering transition and the magnetic effects that result from the structural transition.

II. THERMODYNAMIC MEASUREMENTS

$CsCoO_2$ was synthesized along the azide/nitrate route; details of the procedure have been reported elsewhere [9,10]. Thermodynamic measurements confirm the presence of the reported magnetic transition around $T_N = 424$ K [9]. Differential scanning calorimetry (DSC) measurements on a polycrystalline sample of $CsCoO_2$ were carried out with a DSC device (DSC 404 C, Netzsch GmbH, Selb, Germany) operating in a heat flux mode. The polycrystalline sample is exposed to a linear temperature program and heated at a rate of 10 K/min under streaming dry argon gas up to 600 K. Background contributions were subtracted using external sapphire calibrations. A series of measurements were made consecutively at regular intervals employing an aluminum crucible with a lid, to achieve high reproducibility and precision.

The results of DSC measurements and the Fisher heat capacity method [11] are shown in Fig. 1. The DSC thermogram measured on heating displays an endothermic peak centered around 421 K corresponding to the onset of long-range AFM ordering, in good agreement with the Néel temperature observed by other methods (see below). The rate of temperature change only slightly affects the enthalpy change but does not alter the transition temperature range. There is a substantial change in magnetic entropy and large thermal hysteresis ($\Delta T \approx 15$ K) at T_N between the heating and cooling scans of the DSC plot. In addition, employing the Fisher heat capacity method we have calculated $d(\chi T)/dT$ vs T from

*r.c.williams@durham.ac.uk

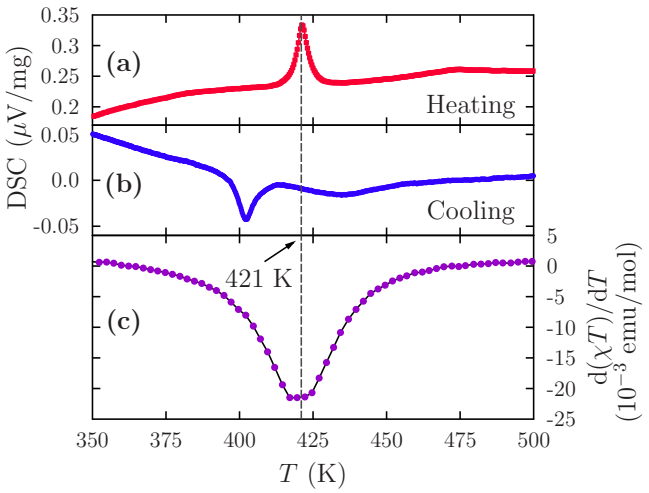

FIG. 1. (Color online) Peaks within the heating (a) and cooling (b) curves in the DSC measurements indicate an enthalpy of transition ΔH associated with the magnetic phase transition around $T \approx 421$ K. (c) The feature in the Fisher heat capacity at $T_N \approx 421$ K verifies the magnetic origin of the transition.

our magnetic susceptibility data [9] as shown in Fig. 1(c), displaying a pronounced minimum consistent with the onset of long-range AFM ordering.

III. NEUTRON POWDER DIFFRACTION

In order to elucidate the magnetic structure below T_N and the details of the structural transition around $T^\star$, neutron powder diffraction (NPD) measurements were made with the High Resolution Powder Diffractometer for Thermal Neutrons, HRPT [12], at SINQ spallation neutron source, at temperatures ranging from 1.5 to 700 K. NPD measurements were made on approximately 2 g of polycrystalline $CsCoO_2$ powder (obtained from six individual batches), enclosed using a graphite sealing in a vanadium cylindrical sample container with diameter of $\approx$6 mm under helium atmosphere. Further NPD experimental information and detailed results from Rietveld refinements are provided in the Appendix.

The NPD patterns collected between 100 and 700 K are consistent with orthorhombic *Cmca* symmetry and can be correctly fitted employing the structural model proposed in our earlier work [9]. Below $T^\star \approx 100$ K a displacive structural phase transition from the high-temperature *Cmca* space group (hereafter the β phase) to monoclinic $C2/c$ space group (hereafter the α phase) is observed as the temperature is reduced, producing a set of new reflections and splitting of certain nuclear intensities accompanying the lowering of symmetry. The structural phase transition is apparent in the temperature dependence of the monoclinic angle β, and is accompanied by a change in slope in the T dependence of the c parameter of the unit cell as depicted in Fig. 2(b). While there are no observable features in the temperature dependencies of the Co-O average distance, and of the Co-O1-Co bond angles via the edges of the CoO_4 tetrahedra, the Co-O2-Co bond angles via the corners of the CoO_4 tetrahedra also reveal the transition: From two distinct angles in the monoclinic α phase, a single one emerges upon entering the orthorhombic β phase, with a value close to

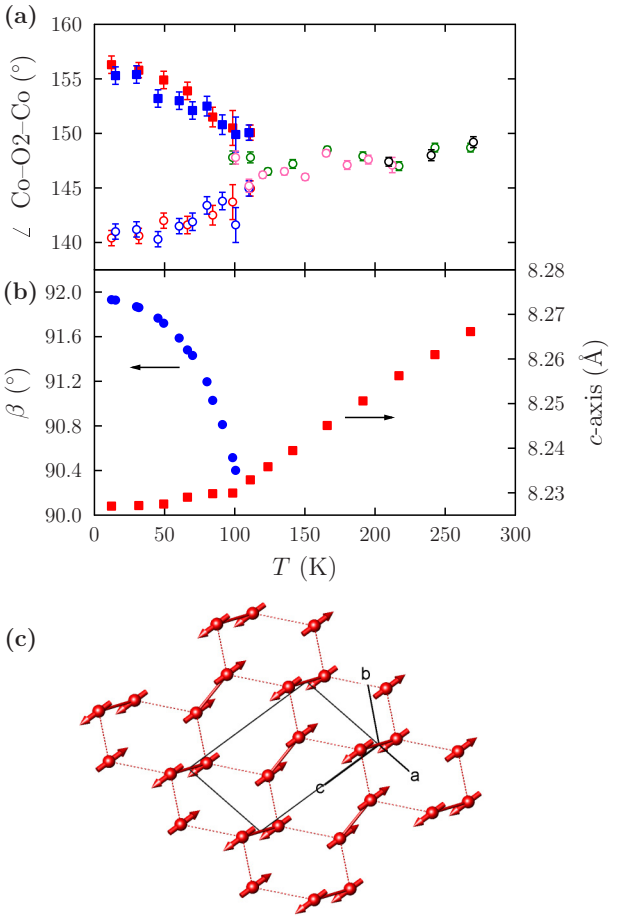

FIG. 2. (Color online) Behavior of the NPD refined nuclear structure for $CsCoO_2$ around the structural phase transition ($T^\star \approx 100$ K): (a) Average Co-O2-Co bond angle involving corner-shared oxygen ions. (b) c axis lattice constant and the monoclinic angle β within α-$CsCoO_2$. (c) Magnetic structure of a single CoO_2 layer within α-$CsCoO_2$.

the mean of the two low-T angles [Fig. 2(a)]. This transition is sharp, but results in no discontinuities in the refined values of the bond angles; they approach each other in a gradual manner with increasing temperature. The refinement of the crystal structures above and below $T_N \approx 430$ K (within the paramagnetic and magnetically ordered phases, respectively) reveals no significant modification in the nuclear structure, indicating this transition is of solely magnetic origin.

At temperatures below 440 K, in both the α and β phases, the NPD patterns of $CsCoO_2$ also contain magnetic diffraction peaks due to the long-range order (LRO) of the magnetic Co^{3+} ion spins. At the structural phase boundary ($T^\star \approx 100$ K), the extra (magnetic) intensities follow the trend of lowering the symmetry; for instance, the magnetic intensity contained in the position of the (1,1,1) peak of the crystal structure in the β phase is split into the extra intensity in the (−1,1,1) and (1,1,1) peaks in the patterns of the α phase below $T^\star$, in a similar fashion to the nuclear intensities. However, no magnetic diffraction pattern changes are observed upon cooling below the structural transition, indicating that the magnetic ordering type and pattern is common to both structural phases. (It is possible that this temperature independence of the average

Co-O bond distances and of the Co-O-Co bond angles via the edge-shared O1 oxygen atoms is what makes the magnetic ordering so robust against the structural phase transition occurring at $T^{\star}$.) All the magnetic diffraction peaks have been indexed with the propagation vector $\boldsymbol{k} = (0,0,0)$, for both the α and β phases. The symmetry analysis for this propagation vector and Co ion locations within both the $C2/c$ and $Cmca$ symmetries, has been carried out with the program SARA*h*-2K [13], and all symmetry-reasonable magnetic ordering schemes have been verified against the Rietveld refinements. For both the β orthorhombic and the α monoclinic phase, just one irreducible representation is compatible with the magnetic ordering model, satisfactorily explaining the observed magnetic intensity patterns. The magnetic ordering is essentially identical for both the α and β phases and is illustrated in Fig. 2(c) for one buckled CoO_2 layer. This spin order consists of ferromagnetically ordered Co-Co dimers, which are themselves antiferromagnetic ordered. The intradimer Co-Co interatomic distance is significantly shorter than the corresponding interdimer Co-Co junctions. In the directions of the closest interdimer distances in the ac planes (along the diagonal $\boldsymbol{a} + \boldsymbol{c}$ and $\boldsymbol{a} - \boldsymbol{c}$ directions), the ordering between the Co moments in the adjacent dimers is antiferromagnetic, thus leading to the overall compensation of the total magnetization. In the adjacent CoO_2 layer, the magnetic ordering repeats, being naturally offset by a (0.5,0.5,0) translation. We find that the direction of the Co^{3+} magnetic moments is along the c axis of the crystal lattice. The irreducible representations leading to this magnetic ordering type are Γ_1 and Γ_5 (in the notation of SARA*h*-2K) for the α monoclinic and β orthorhombic phases of $CsCoO_2$ correspondingly, which in principle do not preclude Co magnetic moment components along the other crystal axes. In the α phase, an admixture of the a component with identical ordering type as for the actual c direction could be possible, while for both the α and β phases, an admixture of the ferromagnetic ordering with the b component could also be symmetrically reasonable. We are unable to assign any significantly meaningful values to the magnitudes of these two ordering types. This means that at all temperatures $T \leqslant T_N$ where $CsCoO_2$ exhibits magnetic LRO, the only definitely confirmed moment direction is along the c axis of the unit cell. We have determined unusually low magnitudes for the ordered magnetic moments of 3.089(2 K) and 2.628(300 K)μ_B/Co^{3+} for α- and β-$CsCoO_2$, respectively. The suppression of the Co^{3+} magnetic moment, as compared to the predicted spin-only value of $4\mu_B$, can be attributed to strong Co($3d$)O($2p$) hybridization.

IV. DENSITY FUNCTIONAL THEORY CALCULATIONS

To further resolve a microscopic picture of the possible static magnetic structures of $CsCoO_2$, we performed a sequence of density functional theory (DFT) total energy calculations using the CASTEP code [14,15]. The density functional plane wave pseudopotential method within the generalized gradient approximation was used as implemented in the CASTEP code. The plane wave basis set (kinetic energy cutoff and k-point sampling) was set such that total energy differences were converged to better than 1 meV/unit cell. The Perdew-Burke-Ernzerhof generalized gradient approximation functional was used for both valence electrons and to generate the ultrasoft pseudopotentials. A systematic search was performed to categorize the possible AFM structures.

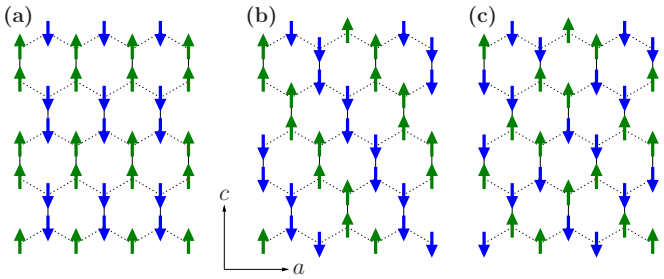

FIG. 3. (Color online) (a) Experimentally observed spin structure formed by the Co ions. (b),(c) Example of higher energy spin structures. The Co ions interact via edge-shared oxygen intradimer (solid line) and corner-shared interdimer (dashed line) superexchange pathways (see main text).

In agreement with the NPD results, the lowest energy configuration for both the α and β phases was found to have strongly ferromagnetically aligned Co-Co dimers, with weaker antiferromagnetic order along the Co chains parallel to the crystallographic a axis [Fig. 3(a)]. The weak AFM interdimer interaction can be easily flipped, as illustrated in Fig. 3(b), at an energy cost of $\Delta E \approx 0.034$ eV/"bond" (for the low-T, α phase). This energy cost may be related to the exchange interaction strength J within the Heisenberg Hamiltonian term for a single exchange bond $\mathcal{H} = -J\boldsymbol{S}_1 \cdot \boldsymbol{S}_2$ (employing the single-J convention) via $\Delta E = (1/2)JS_{\uparrow\uparrow}(S_{\uparrow\uparrow} + 1)$, where $S_{\uparrow\uparrow} = 2S$ is the spin quantum number of the dimer triplet state. For Co^{3+} in the high-spin state, $S = 2$ and therefore $J = \Delta E/10$. Hence the exchange constant for the weak AFM pathway along the corner-shared O^{2-} ion is predicted to be $J' = -39(1)$ K. The ferromagnetic intradimer coupling (via the edge-shared oxygen superexchange pathway) is far stronger. The triplet-singlet energy difference between these Co spins was found to be $\Delta E \approx 0.44$ eV, corresponding to an exchange strength of $J = 511(1)$ K [Fig. 3(c)]. There are a number of possible AFM states analogous to Fig. 3(b) (which preserve the FM intradimer spin configuration) that are close in energy and likely to be populated via thermal fluctuations (see below). Ordered moment sizes (constrained to be collinear) were found to be $3.25\mu_B$ per Co ion, with some spin density transferred onto the edge-shared oxygen ions ($1.2\mu_B$ per ion), in good agreement with the low-T value obtained through NPD refinements.

In order to gain insight into the unusually large intradimer exchange coupling, we have carried out Mulliken analysis by projecting the valence electron wave functions onto an atomic orbital basis set. Our main finding is that, although the corner-shared oxygen sites carry no net spin, the edge-shared oxygens (which link Co ions within a dimer) are significantly spin polarized to $\pm 0.28\hbar$. This is indicative of an enhanced superexchange coupling within the dimers, with one oxygen spin channel having an effective configuration $2p^3$, while the opposite spin channel has $2p^2$.

V. MUON-SPIN RELAXATION

To probe the local magnetism on a time scale distinct from that measured by NPD, muon-spin relaxation (μSR)

measurements [16] were made on $CsCoO_2$. Zero-field μSR measurements were made using the GPS instrument at the Swiss Muon Source. The $CsCoO_2$ powder was loaded into a titanium sample holder in an argon-filled glovebox, covered with 25 μm Ti foil and made airtight with a knife edge seal, and data were collected on heating between 10 and 460 K.

In a μSR experiment, spin-polarized positive muons are implanted into the sample and subsequently decay into a positron with average lifetime $\tau = 2.2$ μs. The decay positron is emitted preferentially in the direction of the muon's instantaneous spin vector. Detectors grouped forward (F) and backward (B) with respect to the muon beam's initial spin polarization direction allow one to measure the positron asymmetry

$$A(t) = \frac{N_{\mathrm{F}}(t) - \alpha N_{\mathrm{B}}(t)}{N_{\mathrm{F}}(t) + \alpha N_{\mathrm{B}}(t)}, \tag{1}$$

where $N_{\mathrm{F,B}}(t)$ are the event histograms at a time t after the muon implantation, and α is an experimental calibration constant. The asymmetry $A(t)$ is proportional to the muon ensemble's spin polarization, the time dependence of which is sensitive to the local magnetic field experienced at the muons' stopping sites.

Spontaneous oscillations in the asymmetry spectra measured in zero field are clearly visible for temperatures below around 420 K [Fig. 4(a)]. This constitutes unambiguous evidence of quasistatic magnetic LRO throughout the bulk of the material. A clear indication of the transition temperature is given by considering the time-averaged ($t \leqslant 9.5$ μs) asymmetry data, which drops abruptly upon cooling, where asymmetry is lost as the material enters the magnetically ordered state. Figure 4(b) shows this drop in average asymmetry, which may be fitted with a Fermi-like step function

$$\langle A \rangle(T) = A_2 + \frac{A_1 - A_2}{e^{(T-T_{\mathrm{c}})/w} + 1}, \tag{2}$$

providing a method for extracting the transition temperature [17] by parametrizing the continuous step from high- (low-) T asymmetry A_2 (A_1) with midpoint T_{c} and width w. The fit yielded values of $T_{\mathrm{c}} = 423.7(2)$ K and $w = 1.57(2)$ K, in agreement with the value previously obtained [9].

Asymmetry spectra below T_{N} were best fitted with the single-frequency oscillatory relaxation function

$$A(t) = A_1 \cos(2\pi \nu t) e^{-\lambda_1 t} + A_2 e^{-\lambda_2 t} + A_{\mathrm{b}}, \tag{3}$$

where the oscillating amplitude A_1 was fixed to its average value of 5.7%. The nonrelaxing baseline contribution A_{b} is attributable to muons which stop in the Ti sample holder, and more importantly, to the nonprecessing component of muon spins which lie parallel to the local magnetic field. Parameters resulting from this fit are displayed in Figs. 4(c) and 4(d).

Upon cooling below T_{N}, the precession frequency ν increases in the expected manner, and the relaxation rates λ_i peak, as is typical for an AFM phase transition (Fig. 4). The Larmor precession frequency of the muon ensemble is related to the average magnitude of the static magnetic field B at the muon site via $2\pi\nu = \gamma B$. Here B, and hence ν serves as an effective order parameter for the LRO. Frequencies in the critical region 400 K $\leqslant T < T_{\mathrm{N}}$ were fitted to $\nu(T) = \nu(0)(1 - T/T_{\mathrm{N}})^{\beta}$, where $T_{\mathrm{N}} = 424$ K was fixed [see Fig. 4(b) inset]. The fit yielded a value for the critical parameter $\beta = 0.35(2)$ [18], which is consistent with that expected for a three-dimensional Heisenberg antiferromagnet. Moreover, dipole field simulations were performed on $CsCoO_2$ using the proposed magnetic spin structure and crystal parameters obtained from x-ray diffraction at 50 and 296 K [9]. A Bayesian analysis of this calculation [19] shows that the observed muon precession frequencies are fully consistent with a moment size of $2.63\mu_{\mathrm{B}}$ from the neutron measurement and further suggests a muon stopping site approximately 1 Å from the corner-shared oxygen ions (see Appendix for further details).

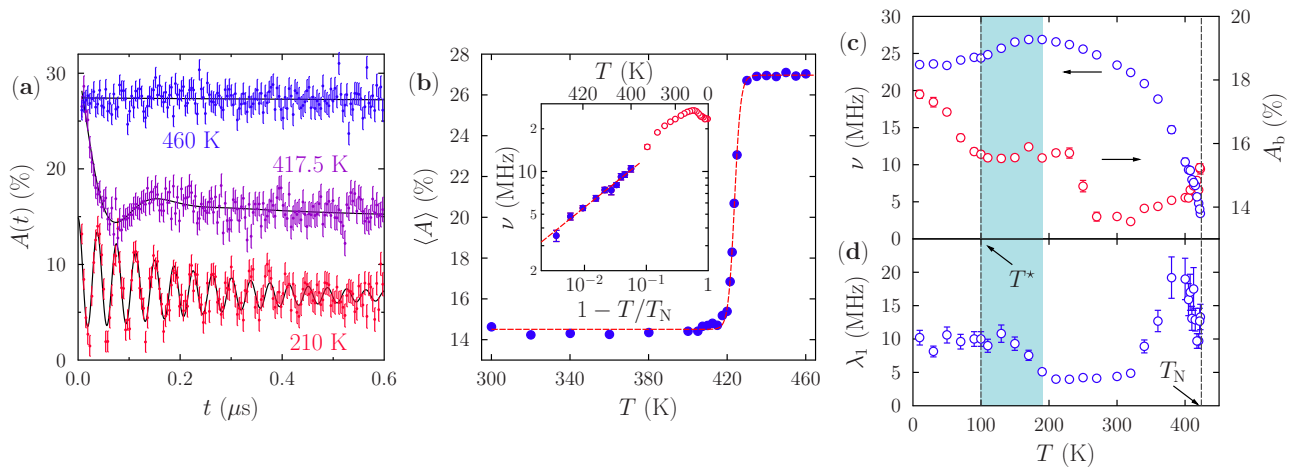

FIG. 4. (Color online) (a) $A(t)$ spectra, showing single-frequency oscillations in the ordered regime with a fit described in the text (the 210 K data are offset by 10% for clarity). (b) Time-averaged asymmetry near the critical region, displaying an abrupt drop in asymmetry $\Delta A = A_2 - A_1$. The dashed line is the fit described in the text. Inset: scaling plot for the order parameter ν. The linear fit indicates the region where the behavior is critical. (c) Fitted parameters to the oscillatory relaxation function for all asymmetry data ($t \leqslant 9.5$ μs) for temperatures $T < T_{\mathrm{N}}$; frequency ν and baseline asymmetry A_{b}, and (d) transverse relaxation rate λ_1. The Néel temperature $T_{\mathrm{N}} = 424$ K and the anomalous temperature region $100 \lesssim T \lesssim 190$ K are indicated.

In addition to the behavior observed around T_N described above, which is quite typical for an AFM transition, we find that on cooling through the region $T < T_N$, there are a number of additional, notable features in the μSR data. We find that on cooling below $\approx$190 K the muon precession frequency ν is smoothly suppressed [Fig. 4(c)]. This is accompanied by a steady increase in λ_1, such that λ_1 is larger by a factor of about 2 below $T^\star$ than in the region 200 K $\lesssim T \lesssim$ 300 K [Fig. 4(d)]. Below $T^\star \approx$ 100 K, λ_1 and ν both level off at constant values. The decrease of ν below 200 K indicates a reduced value of average magnetic field strength experienced at the muon stopping sites. In the fast fluctuation limit we expect that the relaxation rate $\lambda \propto \langle (B - \langle B \rangle)^2 \rangle \tau$ (i.e., the second moment of the magnetic field distribution multiplied by the correlation time τ [20]) and so the additional dephasing indicates a broadening of the distribution of static magnetic field strengths experienced by the muon ensemble, or an increased correlation time as relaxation channels freeze-out on the muon time scale. It is possible that this behavior reflects the the system exploring some of the energetically similar magnetic states predicted by the DFT calculations described above. These states are realized by flipping the overall spin of a dimer, while preserving their FM intradimer spin configuration [Fig. 3(b)]. Although this could conceivably lead the muon ensemble to experience a broader static magnetic field distribution, with a lower mean-field strength, one would expect this to occur below $T^\star$ rather than above it. Moreover, the refined cobalt moment sizes from NPD data [Fig. 6(d) in the Appendix] do not show this suppression below 200 K, suggesting that the effect could be dynamic and related to the issue of time scale. Such effects are therefore not seen in the neutron measurements as these effectively take a "snapshot" of the spin distribution, when compared to the muon GHz time scale.

Additional evidence for the influence of dynamics comes from the baseline asymmetry A_b, which increases abruptly at around 250 K and upon further cooling below $T^\star$ gradually increases further [Fig. 4(c)]. Since relaxation of those muon spins that initially point along the direction of the local magnetic field can only be achieved by dynamic relaxation precesses, the increase of such a nonrelaxing signal is usually indicative of a freezing of relaxation processes. We therefore have evidence for an initial, abrupt freezing of some relaxation channels around 250 K, prefiguring the suppression of the precession frequency ν, with a further, smooth increase below 100 K that seems to track the size of the monoclinic distortion as indicated by both the change in unit cell angle β and the splitting of the corner-shared bond angle Co-O2-Co (Fig. 2). This monoclinic distortion leads to a disproportionation of the corner-shared oxygen bond angles; above $T^\star$ there is one unique value of about 150°, whereas below there appear two classes of bond with angles of around 140° and 155° (bond angles are provided in the Appendix). These values lie within the linear GKA rule regime, but not particularly close to the fully linear angle of 180° (which leads to strong AFM coupling), hence the weaker AFM exchange interaction strength J'. Meanwhile the edge-shared intradimer bond angle only slightly deviates from 90° both above and below $T^\star$ (88° and 86°, respectively) and therefore displays a strong FM superexchange interaction as expected from GKA. The weaker AFM interdimer coupling drives the transition to LRO, and so the system would be sensitive to the bifurcation of the corner-shared oxygen bond angle below $T^\star$, where the AFM exchange interaction strength J' would also split into two unequal values. When these superexchange pathways become inequivalent in the monoclinic phase it is possible that this allows some relaxation channels to freeze-out, leading to a greater static component of the magnetic field, and hence the increase in nonrelaxing asymmetry A_b observed.

VI. CONCLUSION

In conclusion, neutron powder diffraction has enabled the determination of the microscopic magnetic structure of $CsCoO_2$ below the Néel temperature. The tetrahedrally coordinated high-spin ($S = 2$) Co^{3+} ions form a spin configuration comprising strongly FM linked dimers, with weaker AFM interdimer superexchange interactions creating the extended LRO within the extended CoO_2 planes. This spin configuration is observed both above and below a structural phase transition around $T^\star \approx$ 100 K, and is supported by DFT calculations. The bifurcation of bond angles, and hence superexchange pathway interaction strengths pertaining to the weaker AFM interdimer interactions, result in a complicated freezing of relaxation processes on the muon time scale.

ACKNOWLEDGMENTS

Part of this work was carried out at the Swiss spallation neutron source SINQ and Swiss muon source SμS, Paul Scherrer Institut, Villigen, Switzerland. We are grateful for the provision of beam time, and to Alex Amato for muon experimental assistance. We also wish to thank UKCP and the Archer HPC facility for computer time. This work is supported by the EPSRC (UK).

APPENDIX

1. Neutron powder diffraction

As described in the main text, NPD measurements were made with the HRPT instrument at the SINQ spallation neutron source, for $1.5 \leqslant T \leqslant 700$ K. For the temperatures below room temperature (1.5–270 K), a standard orange cryostat was used, the intermediate temperature patterns (at 210–330 K) were collected using the closed-cycle refrigerator with an additional heating stage, while for the temperatures above room temperature, a radiation-type furnace was used. Altogether, five different setups of the instrument optics and sample environment configuration were used.

Lattice constants, atomic coordinates, and hence interatomic distances and angles were systematically refined for all the NPD datasets. At several selected temperatures (1.5, 300, 480, and 700 K) high intensity datasets were collected in order to precisely refine all structural parameters. The structural parameters obtained using Rietveld refinement are consistent with those previously reported, which were obtained using single crystal x-ray scattering [9]. At 1.5, 300, 480, and 700 K high intensity datasets were collected in order to precisely refine all structural parameters. These highest quality datasets always comprised at least one collection with high intensity mode and neutron wavelength $\lambda = 1.494$ Å,

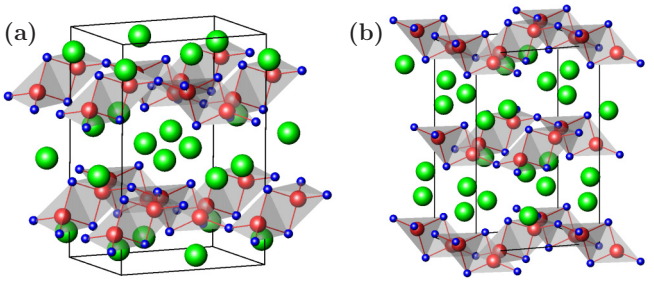

FIG. 5. (Color online) Illustration of the nuclear structure of $CsCoO_2$, depicting (a) the low-temperature monoclinic α phase structure refined at 2 K and (b) the high-temperature orthorhombic β phase refined at 300 K.

and one dataset collected in the medium resolution mode and $\lambda = 1.886$ Å. At all other intermediate temperatures, the data were collected with a neutron wavelength $\lambda = 1.886$ Å and high intensity mode of HRPT. The refinements of the parameters of crystal and magnetic structures were carried out with the FULLPROF suite of programs [21], with the use of its internal tabulated values of the coherent elastic neutron scattering lengths (5.42, 2.49, and 5.803 fm for Cs, Co, and O, respectively), as well as of the magnetic neutron scattering form factors for the magnetic Co^{3+} ion.

Figure 5 provides illustrations of the nuclear structures for both the α (low-temperature, monoclinic) and β (high-temperature, orthorhombic) phases of $CsCoO_2$, as refined from the NPD data. Figures 6(a)–6(c) display examples of the Rietveld refinement fits carried out on the higher statistics datasets. The polycrystalline powder of $CsCoO_2$ contains traces of cobalt(II) oxide, CoO [22–24], and metallic silver [25] particles from the autoclave as an impurity. The impurity contents remained constant ($<5\%$) throughout the analysis, as controlled by the multiphase Rietveld refinement procedures.

The Rietveld refinement of the NPD patterns acquired in the temperature range $1.5 < T < 100$ K, in space group $C2/c$, using the atomic coordinates of α-$CsCoO_2$ as the starting model [9], show a satisfactory agreement between the experimental and calculated nuclear Bragg peaks [see Figs. 6(a) and 6(b)]. The superior quality of refinement for

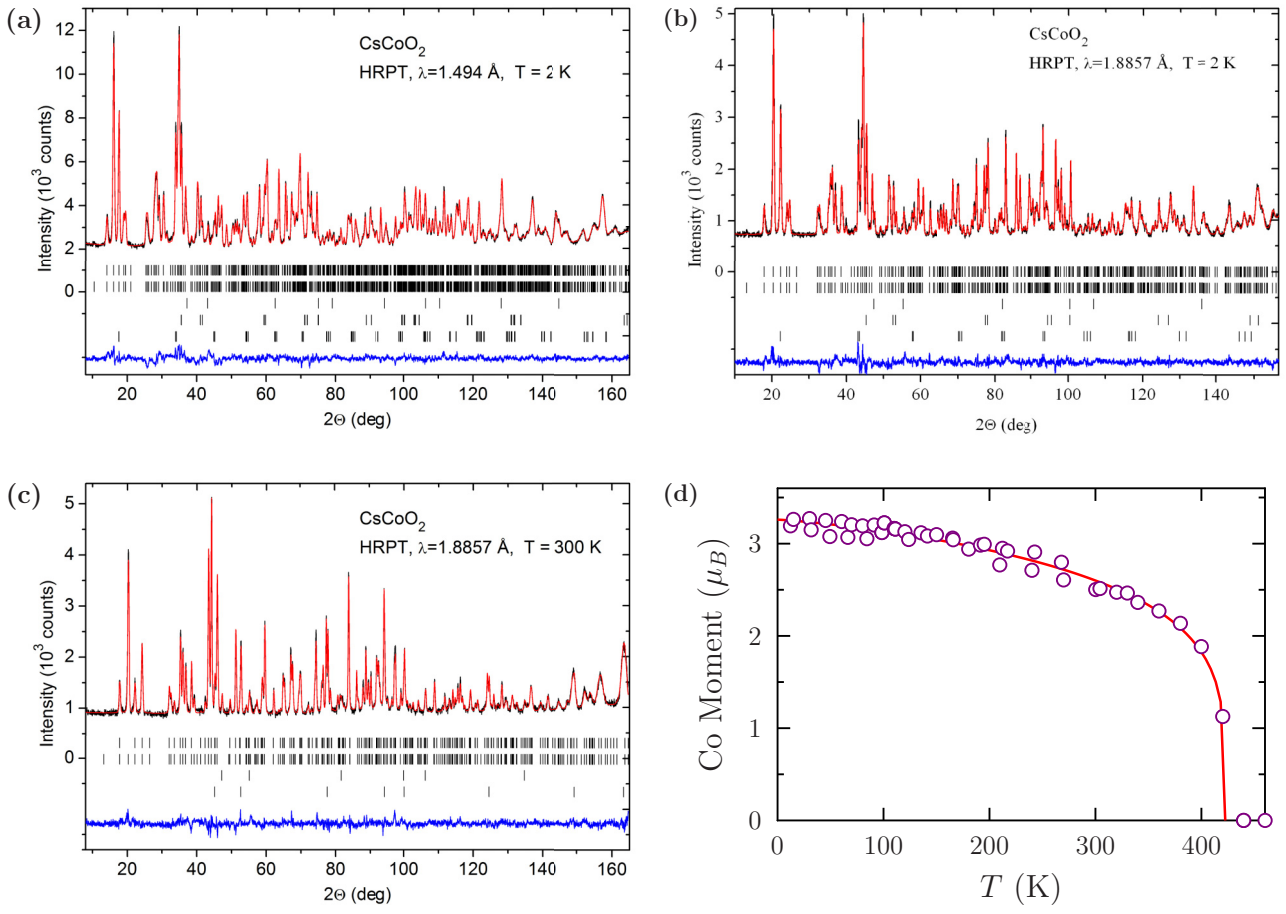

FIG. 6. (Color online) Rietveld refinements of the crystal and magnetic structure of $CsCoO_2$ at [(a), (b)] 2 K (space group $C2/c$) and (c) 300 K (space group $Cmca$), from NPD data collected with (a) $\lambda = 1.494$ Å in the high resolution mode and [(b), (c)] $\lambda = 1.8557$ Å in the medium resolution mode. The observed intensity, calculated profile, and difference curves are shown. The rows of ticks at the bottom of each panel correspond to the calculated diffraction peak positions of the phases (from top to bottom): relevant $CsCoO_2$ nuclear structure, its magnetic phase ($\boldsymbol{k} = 0$), Ag impurity, CoO impurity nuclear structure [monoclinic in (a) and (b) and cubic in (c)], and the magnetic structure of CoO [$\boldsymbol{k} = (0,1,1/2)$ in (a) and (b) only]. (d) Ordered Co^{3+} moment size as obtained by Rietveld refinements of NPD data. The solid line is a guide to the eye.

TABLE I. Refined crystal structure parameters, as well as the Co-O bond lengths and Co-O-Co bond angles, of $CsCoO_2$ refined in space group $C2/c$ at 1.5 K, and in space group $Cmca$ at 300, 480 and 700 K.

	1.5 K	300 K	480 K	700 K
Lattice parameters:				
a (Å)	5.9747(2)	5.9936(2)	6.0028(3)	6.0084(4)
b (Å)	12.2045(5)	12.2529(4)	12.3177(6)	12.4243(8)
c (Å)	8.2324(3)	8.2735(3)	8.3077(4)	8.3532(5)
β (deg)	91.9416(8)			
Bond lengths and angles:				
Co-O1 bonds (Å) (bridging over the O1-O1 edge)	1.885(4) and 1.878(5)	1.879(5) and 1.910(5)	1.894(6) and 1.912(7)	1.881(7) and 1.905(7)
Co-O2.O3 bonds (Å) (bridging through the corners)	1.826(4) and 1.825(4)	2 × 1.811(3)	2 × 1.805(3)	2 × 1.814(3)
Co-Co intradimer (Å)	2.576(7)	2.628(6)	2.653(7)	2.633(8)
Co-Co interdimer (Å)	3.433(6) and 3.565(6)	3.495(3)	3.488(4)	3.510(4)
Co-O1-Co angles (deg) (bridging over the edge)	86.4(3)	87.9(3)	88.4(4)	88.1(5)
Co-O2-Co angles (deg) (bridging through the corner)	140.1(4)	149.6(2)	150.1(3)	150.8(3)
Co-O3-Co angles (deg) (bridging through the corner)	155.3(4)			

datasets collected using $\lambda = 1.494$ Å may be seen by comparing these plots. The neutron diffraction patterns collected between $100 < T < 700$ K are consistent with orthorhombic $Cmca$ symmetry and may also be correctly fitted employing the structural model proposed earlier via our single crystal x-ray measurements [9]. The good agreement between the calculated and observed patterns is presented in Fig. 6(c). Figure 6(d) shows the temperature dependence of the ordered moment size of the cobalt ions below T_N, as refined from the NPD data. Refined crystal structure parameters (together with bond distances and angles) for both phases of $CsCoO_2$ are presented in Table I, as obtained using high intensity NPD. Atomic coordinates and isotropic thermal displacement parameters for β- and α-$CsCoO_2$ are presented in Tables II and III, respectively.

TABLE II. Atomic coordinates and isotropic thermal displacement parameters for β-$CsCoO_2$ at selected temperatures.

		300 K	480 K	700 K
Atom, site:				
Cs, $8f(0,y,z)$,	y	0.3361(2)	0.3365(2)	0.3354(2)
	z	0.0733(3)	0.0753(4)	0.0733(5)
	B (Å^2)	1.29(5)	2.05(6)	3.42(9)
Co, $8f(0,y,z)$,	y	0.0489(4)	0.0479(5)	0.0469(5)
	z	0.1413(5)	0.1430(6)	0.1413(7)
	B (Å^2)	1.00(7)	1.81(9)	2.74(13)
O1, $8f(0,y,z)$,	y	0.0999(2)	0.0996(2)	0.0988(2)
	z	−0.0726(3)	−0.0716(4)	−0.0703(4)
	B (Å^2)	1.36(5)	2.04(6)	2.95(7)
O2, $8f(\frac{1}{4},y,\frac{1}{4})$,	y	0.0874(2)	0.0857(3)	0.0837(3)
	B (Å^2)	1.70(5)	2.63(7)	3.87(9)

2. Bayesian analysis

The dipolar field $\mathbf{B}_{\rm dip}(\mathbf{r}_\mu)$ at a muon stopping site $\mathbf{r}_\mu$ due to the coupling with localized magnetic moments $\mathbf{m}_i$ located at positions $\mathbf{r}_i$ is given by

$$\mathbf{B}_{\rm dip}(\mathbf{r}_\mu) = \frac{\mu_0}{4\pi}\sum_i \frac{3(\mathbf{m}_i\cdot\hat{\mathbf{r}}_{i\mu})\hat{\mathbf{r}}_{i\mu} - \mathbf{m}_i}{|\mathbf{r}_\mu - \mathbf{r}_i|^3}, \qquad \text{(A1)}$$

where μ_0 is the vacuum permeability and $\hat{\mathbf{r}}_{i\mu}$ is the normalized vector between the muon and the moment $\mathbf{m}_i$. The dipolar interaction may be evaluated for an infinite sample by calculating the magnetic field given by Eq. (A1) within a

TABLE III. Atomic coordinates and isotropic thermal displacement parameters for α-$CsCoO_2$ refined at 1.5 K.

Atom, site:		
Cs, $8f(x,y,z)$,	x	0.2556(4)
	y	0.0868(2)
	z	0.5722(3)
	B (Å^2)	0.13(4)
Co, $8f(x,y,z)$,	x	0.2487(7)
	y	0.2981(3)
	z	0.8607(6)
	B (Å^2)	0.27(6)
O1, $8f(x,y,z)$,	x	0.2438(4)
	y	0.1499(2)
	z	0.9245(3)
	B (Å^2)	0.22(3)
O2, $4e(0,y,\frac{1}{4})$,	y	0.6508(3)
	B (Å^2)	0.21(5)
O3, $4e(0,y,\frac{1}{4})$,	y	0.1699(3)
	B (Å^2)	0.46(6)

Lorentz sphere of finite radius r_L. The Lorentz sphere needs to be sufficiently large to reach satisfactory convergence of the calculated field. In our calculations $r_L = 42$ Å. As only antiferromagnetic structures were considered, no further terms need to be considered for the diamagnetic muon sites.

If the magnetic field experienced by the muon is entirely dipolar (i.e., we neglect the contact hyperfine field), then the magnetic field calculated at any given site is proportional to the precession frequency of a muon situated there. Therefore we may obtain the frequency (per unit moment size) probability density function (PDF) $f(\nu/\mu)$, both for the entire unit cell, and for a reduced volume fraction satisfying physically justified constraints on muon sites. The constraints applied were that a muon typically lies 1 Å away from an oxygen ion [26] ($0.9 \leqslant r_1 \leqslant 1.1$ Å) and will not come to rest too close to a positively charged ion ($r_2 \geqslant 1$ Å). Using Bayesian inference together with the observed precession frequency [19], one is able to find the PDF for the ordered moment size:

$$g(\mu|\nu) = \frac{\frac{1}{\mu} f(\nu/\mu)}{\int_0^{\mu_{\max}} \frac{1}{\mu'} f(\nu/\mu')\, d\mu'}, \tag{A2}$$

where the prior moment size distribution has been taken to be a uniform probability between zero and $\mu_{\max}$ (calculations are insensitive to the value chosen as long as it exceeds any conceivable value deduced by prior reasoning, which here is $10\mu_B$).

The observed precession frequency [Fig. 4(c)] at both 50 K (α phase) and 300 K (β phase) was 23.4 MHz. Neutron data indicates that the ordered moment size is $2.63\mu_B$ at 296 K, and hence this value was used to scale the frequency PDF shown in Fig. 7(a). The observed frequency $\nu = 23.4$ MHz is labeled, and the PDF has a clear peak lying very close to this value. Using this value of ordered moment size, a candidate muon site was located which lies approximately 1 Å from the corner-sharing oxygen ions, on the outside of the Co-O-Co angle, which would give rise to the observed muon precession frequency. The ordered moment size PDFs $g(\mu|\nu)$ are displayed in Fig. 7(b), and there are peaks positioned very close to the indicated moment size of $2.63\mu_B$ within both the α and β phases. The fact that all PDFs generated are remarkably similar for the monoclinic α and orthorhombic β phases suggests that the impact of the structural transition on the muon stopping site location (and hence local magnetic field strength) is not severe, and is therefore unlikely to be the sole cause of the suppression of the order parameter observed around $T^\star$.

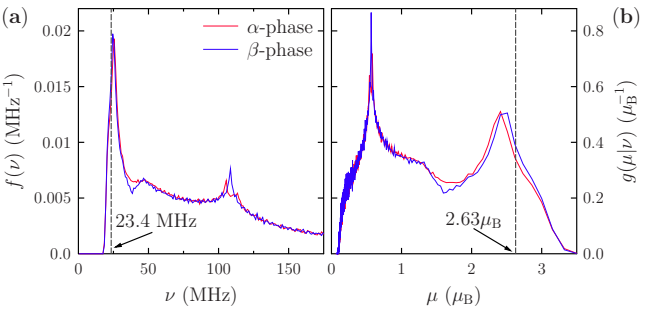

FIG. 7. (Color online) (a) Precession frequency PDF (scaled for an ordered moment size $\mu = 2.63\mu_B$). (b) Ordered moment size PDF, obtained using the observed precession frequency $\nu = 23.4$ MHz. Data are constrained to a limited volume fraction of the unit cell, as described in the text.

[1] A. Maignan, C. Michel, A. C. Masset, C. Martin, and B. Raveau, Eur. Phys. J. B **15**, 657 (2000).

[2] J. B. Goodenough, *Progress in Solid State Chemistry*, edited by H. Reiss (Pergamon, Oxford, 1965), Vol. 5, p. 145.

[3] M. Pouchard, A. Villesuzanne, and J.-P. Doumerc, J. Solid State Chem. **162**, 282 (2001).

[4] M. Jansen and R. Hoppe, Z. Anorg. Allg. Chem. **417**, 31 (1975).

[5] C. Delmas, C. Fouassier, and P. Hagenmuller, J. Solid State Chem. **13**, 165 (1975).

[6] M. Sofin, E. M. Peters, and M. Jansen, J. Solid State Chem. **177**, 2550 (2004).

[7] J. Birx and R. Hoppe, Z. Anorg. Allg. Chem. **597**, 19 (1991).

[8] N. Stüßer, M. Sofin, R. Bircher, Hans-Ulrich Güdel, and M. Jansen, Chem. Eur. J. **12**, 5452 (2006).

[9] N. Z. Ali, J. Nuss, R. K. Kremer, and M. Jansen, Inorg. Chem. **51**, 12336 (2012).

[10] M. Jansen, Z. Anorg. Allg. Chem. **638**, 1910 (2012).

[11] M. E. Fisher, Philos. Mag. **7**, 1731 (1962).

[12] P. Fischer, G. Frey, M. Koch, M. Könnecke, V. Pomjakushin, J. Schefer, R. Thut, N. Schlumpf, R. Bürge, U. Greuter, S. Bondt, and E. Berruyer, Physica B **276–278**, 146 (2000).

[13] A. S. Wills, Physica B **276-278**, 680 (2000); program available from www.ccp14.ac.uk.

[14] S. J. Clark, M. D. Segall, C. J. Pickard, P. J. Hasnip, M. I. J. Probert, K. Refson, and M. C. Payne, Z. Kristallogr. **220**, 567 (2005).

[15] P. J. Hasnip, K. Refson, M. I. J. Probert, J. R. Yates, S. J. Clark, and C. J. Pickard, Philos. Trans. R. Soc. A **372**, 20130270 (2014).

[16] S. J. Blundell, Contemp. Phys. **40**, 175 (1999).

[17] A. J. Steele, T. Lancaster, S. J. Blundell, P. J. Baker, F. L. Pratt, C. Baines, M. M. Conner, H. I. Southerland, J. L. Manson, and J. A. Schlueter, Phys. Rev. B **84**, 064412 (2011).

[18] The value of the critical parameter β for a given fitted frequency ν was found to be sensitive to the time range over which the asymmetry spectra were fitted. The quoted value of 0.35 was obtained for fits over early times only ($t \leqslant 1$ μs), which are most sensitive to the behavior of the oscillations.

[19] S. J. Blundell, A. J. Steele, T. Lancaster, J. D. Wright, and F. L. Pratt, Phys. Procedia **30**, 113 (2012).

[20] R. S. Hayano, Y. J. Uemura, J. Imazato, N. Nishida, T. Yamazaki, and R. Kubo, Phys. Rev. B **20**, 850 (1979).

[21] J. Rodríguez-Carvajal, Physica B **192**, 55 (1993).
[22] G. Natta and A. Reina, An. Fis. Quim. **24**, 611 (1926).
[23] W. Jauch, M. Reehuis, H. J. Bleif, F. Kubanek, and P. Pattison, Phys. Rev. B **64**, 052102 (2001).
[24] K. Tomiyasu, T. Inami, and N. Ikeda, Phys. Rev. B **70**, 184411 (2004).
[25] I. K. Suh, H. Ohta, and Y. Waseda, J. Mater. Sci. **23**, 757 (1988).
[26] J. H. Brewer, R. F. Kiefl, J. F. Carolan, P. Dosanjh, W. N. Hardy, S. R. Kreitzman, Q. Li, T. M. Riseman, P. Schleger, H. Zhou, E. J. Ansaldo, D. R. Noakes, L. P. Le, G. M. Luke, Y. J. Uemura, K. Hepburn-Wiley, and C. E. Stronach, Hyperfine Interact. **63**, 177 (1991).